

Eulerian-Lagrangian simulation of pulverized biomass jet using spheroidal particle approximation

Ning Guo¹, Tian Li^{1,*}, Lihao Zhao^{2,1}, Terese Løvås¹

¹Department of Energy and Process Engineering, Faculty of Engineering, NTNU - Norwegian University of Science and Technology, Trondheim, Norway

²Department of Engineering Mechanics, Tsinghua University, Beijing, China

*Corresponding author, email: tian.li@ntnu.no

Abstract

Pulverized biomass has great potential to replace coal in the many industrial systems such as suspension-firing furnace and entrained-flow gasifier. The shape of pulverized biomass deviates significantly from the quasi-spherical coal particle. However, it is common to simulate pulverized biomass particles as spheres as most biomass models are developed based on coal models. With the aim to obtain a more realistic simulation of pulverized biomass, this work extends the treatment of pulverized biomass to spheroids. A spheroid model that accounts for spheroidal particle drag force and torque is implemented into an Eulerian-Lagrange computational fluid dynamic solver. Comprehensive verifications and validations are performed by comparing with experiments and direct numerical simulations. Furthermore, non-reactive simulations of a lab-scale entrained flow gasifier are carried out using both the conventional spherical particle model, simplified non-sphere model, and the implemented detailed spheroidal particle model. By studying the simulation results of particle and fluid velocities in axial, radial and tangential directions, differences are observed when comparing the sphere model, the simplified non-sphere model, and the spheroid model. The spheroid model also indicates that particle orientation, which is ignored in the sphere model and the simplified non-sphere model, plays a role in the behavior of the particle dynamics. It is also found that, under such conditions, the spheroid model, compared to the sphere model, yields a more dispersed distribution regarding the particle residence time and local concentration. These non-reactive simulation results imply that shortcomings may exist in the common practice of simulating conversion of pulverized biomass in which the sphere model or the simplified non-sphere model is applied.

28 **Keywords:** spheroidal particle, pulverized biomass, CFD, entrained flow gasifier, OpenFOAM

29

30 1. Introduction

31 In order to address the increasing concerns related to the use of fossil fuels for both heat and power
32 as well as fuel production [1], it is of interest to investigate the sustainable use of alternative fuels to
33 replace traditional fossil fuels. One viable option is to utilize biomass. For example, liquid biofuels can
34 be produced via entrained flow gasification. In this process, pulverized biomass is gasified in an
35 entrained flow gasifier and the produced bio-syngas is further converted into liquid hydrocarbons by
36 Fischer-Tropsch synthesis [2].

37 Due to the fibrous nature of bio-based feedstock, pulverized biomass particles come in various
38 shapes. For example, scanning electron microscope images of Norwegian spruce and forest residuals
39 show that particles are mainly large needle-like oblongs [3]. Gubba et al. [4] presented electron
40 microscopy images of milled wood and palm kernel expeller and showed particle shapes varying from
41 cylinders, spheres, slabs and other irregular shapes. Panahi et al. [5] published optical microscope
42 photographs of pulverized Miscanthus and Beechwood particles and showed that most of them are
43 cylinder-like in shape. Despite the shape of pulverized biomass particles being non-spherical, the
44 majority of research up until recently use spheres to represent pulverized biomass particles in
45 computational fluid dynamic (CFD) simulations [6][7][8]. This simplification may lead to several
46 problems related to the predictability of such models for larger applications. To begin with, given the
47 same flow field, spherical and non-spherical particles have different hydrodynamic behavior due to the
48 difference in hydrodynamic drag and torque. Drag forces are dependent on particle cross-sectional areas
49 projected to flow directions. Values of the particle cross-sectional projected area vary in the case of non-
50 spheres as they will rotate, but cross-sectional projected areas remain constant for spheres. Furthermore,
51 particle torques, which are often ignored in simulations of spheres due to central symmetry, have to be
52 included in simulations when particles are non-spherical to account for particle rotations. In addition to
53 hydrodynamic considerations, the particle heat and mass transfer of non-spheres are likely to be different
54 from spheres. These are all factors that have influence on particle trajectories, residence times, heat
55 transfer, and temporal developments of particle conversion. Without considering these aforementioned

56 effects, simulations employing the spherical particle assumption would fail to capture details of the
57 thermal conversion of pulverized biomass observed in experiments.

58 To remedy these issues, efforts have been made to investigate the behavior of non-spherical particles
59 in flow systems. From particle hydrodynamics perspective, Zhang et al. [9] carried out numerical
60 investigations of particle dispersion in detail and found that particle shapes affects the dispersity.
61 Wachem et al. [10] simulated spherical, ellipsoidal, disc and fiber shaped particles in turbulent channel
62 flow with large Stokes numbers and mass loading factor of unity. Their study shows that non-spherical
63 particles are most stable when their longest axes are perpendicular to the flow, which makes them having
64 higher average velocities than spherical particles with equivalent volume. These works all contributed
65 to the understanding of the differences of dynamics between spherical and non-spherical particles. One
66 important force affecting the dynamics of a non-spherical particle is the drag force. Numerical studies
67 on modelling drag forces of non-spherical particles can be generally classified into two categories. The
68 first approach is to use simple shape factors (such as particle sphericity) to account for the irregular
69 shapes of non-spherical particles and then to modify the drag coefficients based on the said shape factors.
70 However, such method does not consider the effects of particle orientations. A typical example of this
71 approach is the simplified non-sphere model developed by Haider and Levenspiel [11], which has been
72 implemented into many mainstream CFD solvers including Ansys Fluent and OpenFOAM. This is one
73 of the most commonly used model that takes account the shape of a particle and has been used in a
74 handful CFD studies of modelling biomass [12][13]. Another approach of modelling the drag forces of
75 non-spherical particle is to include the effects of particle orientations. This could be done either by
76 introducing inclination angle (angle between particle major axis and flow direction) as in the work of
77 Rosendahl [14] or making particle sphericity or drag coefficient dependent on particle orientations as in
78 the work of Hölzer and Sommerfeld [15]. In addition, attention has been paid to heat and mass transfer
79 processes of non-spherical particles. Schiemann et al. [16] studied particle shape effects on char burning
80 kinetics using imaging pyrometry, and it was concluded that particle shapes should be taken into account,
81 otherwise it could leads to miss-interpretation of char burning rate. Vorobiev et al. [17] further included
82 the influence of Stefan flow to study burning rates of torrefied biomass. A comprehensive model for
83 char burnout kinetic that considers Stefan flow effects was presented in their paper. They reported that

84 effects of Stefan flow are more pronounced in small particles with large aspect ratios. Grow [18]
85 investigated heat and mass transfer for an ellipsoidal particle and showed that, in the case of diffusion
86 controlled combustion, the average combustion rate of ellipsoidal particles are only slightly higher than
87 spherical particle of the same surface area. This is confirmed by Li and Zhang [19] who conducted a
88 theoretical study on spheroidal char particles under forced convection conditions and it was found that,
89 in both diffusion controlled and diffusion-kinetic controlled cases, combustion rates increase with
90 particle aspect ratios.

91 Although there is significant progress in research on simulating particles of non-spherical shape,
92 studies concerning particle-laden jets using detailed description of spheroidal particle models in a reactor
93 for thermochemical conversion of biomass are rare. To better simulate entrained flow gasification of
94 pulverized biomass, a cold flow study with a more realistic approximation of the particle shape is hereby
95 presented as a first step in this work. A spheroid model is implemented into a Eulerian-Lagrangian CFD
96 solver using the open source CFD platform, OpenFOAM [20]. In this spheroid model, pulverized
97 biomass particles are treated as needle-like spheroids. The drag force and torque acting on the particle
98 are all taken into account. Since the proposed CFD solver includes particle torque calculations, the
99 effects of particle orientations can be studied. This makes the proposed spheroid model different than
100 other CFD studies works where biomass particles as are simulated as non-spheres but particle
101 orientations are not considered [12][13]. Furthermore, although the general trend of particle motions by
102 assuming pulverized biomass particles as spheroids instead of spheres is easy to predict by qualitative
103 analysis, quantitative information of differences between these approaches are rarely found in open
104 literatures. The current research meets this need by presenting a comprehensive comparison of particle
105 dynamics calculated from different models.

106 The logical development of this work and the structure of this paper is as follows. The theoretical
107 foundation is explained in Section 2. In Section 3, the verifications and validations of the implemented
108 spheroid model are discussed in two parts: torque and drag. With the validated model, cold flow
109 simulations of a simplified entrained flow gasification reactor are executed in Section 4, where particle
110 and fluid velocities in axial, radial and tangential directions are analyzed and results are compared

111 among those of the sphere model, the simplified non-sphere model and the spheroid model. Particle
112 residence times and concentrations are also studied. Finally, Section 5 summarizes the conclusions.

113

114 **2. Mathematical modelling**

115 Eulerian-Eulerian and Eulerian-Lagrangian models are often employed when simulating dispersed
116 two-phase flows [21]. Eulerian-Eulerian models treat all phases, including particles or particle bundles,
117 as continuous phases and their momentum and continuity equations are solved for each phase [21]. This
118 approach greatly saves computational cost but cannot provide information of any specific particle or
119 particle bundle [21]. Different from Eulerian-Eulerian models, Eulerian-Lagrangian models treat only
120 the fluid phase as continuous phase but the dispersed phase is treated as discrete phase [22]. As a result,
121 an Eulerian-Lagrangian approach is chosen in this study in order to investigate particle behavior on both
122 collective and individual levels. When Eulerian-Lagrangian models are applied, one important aspect
123 that should be considered is the coupling between the continuous phase and the dispersed phase, namely
124 one-way, two-way or four-way coupling; one-way coupling only accounts for the influence of the fluid
125 on the particles, but neglects the particles influence on the fluid and intra-particle interactions; two-way
126 coupling considers the interactions between the fluid and the particles, but neglects the intra-particle
127 interactions; four-way coupling includes interactions between the particles and the fluid, as well as intra-
128 particle interactions [23]. The method of coupling in the present work is explained in Section 2.4. Below
129 outlines the theory of particle models accounting for the drag force and torque used in this work. It
130 should be noted that only drag and buoyant (including gravity) forces that act on the particles are
131 considered in this work. Other forces such as virtual mass force are neglected as they are not important
132 under conditions of interest where particles are relatively small and particle to fluid density is large [23].

133

134 **2.1. The sphere model**

135 Various drag models are available in open literature, for example the distorted sphere drag model by
136 Liu et al. [24]. Here, the following sphere drag model (originally implemented in OpenFOAM [20] 4.x
137 “SphereDragForce.C”, based on [23] with modifications) is used as an example to represent the common
138 practice that pulverized biomass particles are simulated as spheres in CFD.

139 In this particle drag model, the drag force is defined as,

$$140 \quad F_D = \frac{\frac{3}{4}m_p\mu_f C_D(U_f - U_p)}{\rho_f D_p^2} \quad (1)$$

$$141 \quad C_D = \begin{cases} 0.424Re_p, & Re_p < 1000 \\ 24 \left(1 + \frac{1}{6}Re_p^{\frac{2}{3}}\right), & Re_p \geq 1000 \end{cases} \quad (2)$$

$$142 \quad Re_p = \frac{|u_f - u_p|D_p}{\nu_f}, \quad (3)$$

143 where F_D is particle drag force [N], m_p is particle mass [kg], μ_f is fluid dynamic viscosity [$\text{N}\cdot\text{s}/\text{m}^2$], C_D
144 is drag force coefficient, U_f is fluid velocity [m/s], U_p is particle velocity [m/s], ρ_f is fluid density [$\text{kg}/$
145 m^3], D_p is particle diameter [m], Re_p is particle Reynolds number and ν_f is fluid kinematic viscosity
146 [m^2/s]. Note that the torque acting on the spherical particle is not calculated, so the rotation of particle
147 is not considered.

148

149 2.2. The simplified non-sphere model

150 As previously stated, one of the most commonly used model that takes account the shape of a
151 particle is the simplified non-sphere model developed by Haider and Levenspiel [11]. This simplified
152 non-sphere model introduces a so-called shape factor (particle sphericity) to differentiate particle shapes,
153 which is defined as the ratio of surface area of a sphere of equivalent volume to surface area of the non-
154 spherical particle. Four model coefficients B_1 , B_2 , B_3 and B_4 are calculated based on this particle
155 sphericity. The drag force coefficient then is formulated as:

$$156 \quad C_D = \frac{24}{Re} (1 + B_1 \cdot Re^{B_2}) + \frac{Re \cdot B_3}{Re + B_4}, \quad (4)$$

157 Although this model accounts for particle shapes, it still does not consider the orientations of the particle.

158

159 2.3. Spheroid model

160 In analytical geometry, a spheroid at origin point aligned along the coordinates can be described by

$$161 \quad \frac{x^2}{a^2} + \frac{y^2}{a^2} + \frac{z^2}{c^2} = 1. \quad (5)$$

162 The aspect ratio is defined as $\lambda = \frac{c}{a}$ and a and c are the particle axial lengths [m]. A spheroid is referred
163 to as a prolate ellipsoid when its aspect ratio is larger than one and an oblate ellipsoid when its aspect

164 ratio is less than one. When its aspect ratio equals to one, it regresses to a sphere. In this work, the term
165 spheroid is used to referred to a prolate ellipsoid specifically. This correlates to the fact that pulverized
166 biomass particles are usually needle-like and have large aspect ratios [3].

167 When particles are non-spherical, it is of importance to include the particle rotation effects. Therefore,
168 using an appropriate method to describe rotation in three-dimensional space is necessary. Three different
169 Cartesian coordination frames in combination with an Euler rotation theorem are routinely used in
170 previous studies for ellipsoid particles [25][26][27]. The three Cartesian frames are given as follows;
171 $\mathbf{x} = (x_1, x_2, x_3)$ is the inertial frame, $\mathbf{x}' = (x'_1, x'_2, x'_3)$ is the particle frame with its origin at the particle
172 center and its principal axes being the spheroid particle's principle axes. In addition, the co-moving
173 frame, $\mathbf{x}'' = (x''_1, x''_2, x''_3)$, represents the frame whose origin is at the particle center but its axes are
174 parallel to its corresponding axes of the inertial frame.

175 According to Euler's rotation theorem, any rotation in a three-dimensional space can be defined by
176 three angles, referred as Euler's angles. One set of three Euler's angles corresponds to one set of four
177 Euler parameters, (e_0, e_1, e_2, e_3) , and vice versa [28]. The transformation matrix, \mathbf{A} , that can convert
178 between co-moving frame and particle frame is [29] given by:

$$179 \quad \mathbf{x}' = \mathbf{A}\mathbf{x}'' \quad (6)$$

180

181 2.3.1. Drag force of spheroid

182 In this work, the drag model developed by Hölzer and Sommerfeld [15] for spheroid particles is
183 employed. Formulas for drag force and drag force coefficient are given as follows:

$$184 \quad F_D = \frac{1}{2} C_D \rho_f A_c (U_f - U_p) |U_f - U_p| \quad (7)$$

$$185 \quad C_D = \frac{8}{Re_p} \frac{1}{\sqrt{\phi_{\parallel}}} + \frac{16}{Re_p} \frac{1}{\sqrt{\phi}} + \frac{3}{\sqrt{Re_p}} \frac{1}{\phi^{\frac{3}{4}}} + 0.4240^{0.4(-\log \phi)^{0.2}} \frac{1}{\phi_{\perp}}, \quad (8)$$

186 where A_c is particle cross-sectional area that is projected to the flow direction [m^2]. In addition, ϕ , ϕ_{\parallel}
187 and ϕ_{\perp} represent sphericity, lengthwise sphericity and crosswise sphericity, respectively. They account
188 for different particle shapes and orientations. Their detailed definitions can be found in the original
189 reference [15]. The model is implemented in a way that includes sideward motion due to particle major

190 axis being inclined to flow direction (also known as “profile lift” in Mandø and Rosendahl [30]). Particle
191 drag forces are calculated separately in the x -, y - and z -direction in particle frame then are assembled
192 together as vectors in inertia frame, by that particle drag coefficients are calculated separately in the x -,
193 y - and z -direction in particle frame according to Eq. (8). As a result, the directions of assembled drag
194 force vectors in inertia frame could be different from particle-to-fluid slip velocities. It should be noted
195 that Hölzer and Sommerfeld [15] states that this formula considers particle orientations over the entire
196 range of Reynolds numbers up to the critical Reynolds number, whose precise definition is not given in
197 their paper. The model has therefore some shortcomings at certain high Reynolds conditions, which
198 however will not be relevant in the present study.

199

200 2.3.2. Torque of spheroid

201 Particle rotations are governed by [26]:

$$202 \quad I'_{ij} \frac{d\omega'_j}{dt} - \epsilon_{ijk} \omega'_j I'_{kl} \omega'_l = N'_i, \quad (9)$$

203 where I is particle moment of inertia [$\text{kg}\cdot\text{m}^2$], ω is particle angular velocity [rad/s], t is time [s], N is
204 particle torque [$\text{N}\cdot\text{m}$], superscript $'$ refers to the aforementioned frame \mathbf{x}' , ϵ is the Levi-Civita symbol
205 and subscript i, j, k refer to tensor notation indices.

206 There are different ways to model particle torques. For example, two types of torques were
207 considered in the work of Mandø and Rosendahl [30]. The first one is due to resistance and the second
208 one is to offset the pressure center in relation to the geometry center of the particle. Both types of torques
209 are coupled with particle forces in their work. In the present work, an alternative approach is used where
210 particle torques are decoupled from particle forces and it is assumed that the particle geometry center is
211 the pressure center. As a result, torque formulas that can predict particle rotation to a satisfactory extent
212 without coupling with particle forces are required.

213 In this research, particle torques are calculated using formulas developed by Jeffery [31], which are
214 decoupled from particle forces for an ellipsoid in creeping flow (i.e. $Re_p < 1$) [32]:

$$215 \quad N'_x = \frac{16\pi\mu a^3 \lambda}{3(\beta_0 + \lambda^2 \gamma_0)} \left[(1 - \lambda^2) d'_{zy} + (1 + \lambda^2) (w'_{zy} - \omega'_x) \right] \quad (10)$$

$$216 \quad N_y' = \frac{16\pi\mu a^3\lambda}{3(\alpha_0 + \lambda^2\gamma_0)} \left[(\lambda^2 - 1)d_{xz}' + (1 + \lambda^2)(w_{xz}' - \omega_y') \right] \quad (11)$$

$$217 \quad N_z' = \frac{32\pi\mu a^3\lambda}{3(\alpha_0 + \lambda^2\beta_0)} (w_{yx}' - \omega_z'), \quad (12)$$

218 where strain rate [s⁻¹] is

$$219 \quad d_{ij}' = \frac{1}{2} \left(\frac{\partial U_i'}{\partial x_j'} + \frac{\partial U_j'}{\partial x_i'} \right) \quad (13)$$

220 fluid rotation tensor [s⁻¹] is

$$221 \quad w_{ij}' = \frac{1}{2} \left(\frac{\partial U_i'}{\partial x_j'} - \frac{\partial U_j'}{\partial x_i'} \right) \quad (14)$$

222 and α_0 , β_0 and γ_0 are dimensionless parameters given by Gallily and Cohen [33]:

$$223 \quad \alpha_0 = \beta_0 = \frac{2\lambda^2(\lambda^2-1)^{\frac{1}{2}} + \lambda \ln \left[\frac{\lambda - (\lambda^2-1)^{\frac{1}{2}}}{\lambda + (\lambda^2-1)^{\frac{1}{2}}} \right]}{2(\lambda^2-1)^{\frac{3}{2}}} \quad (15)$$

$$224 \quad \gamma_0 = \frac{2(\lambda^2-1)^{\frac{1}{2}} + \lambda \ln \left[\frac{\lambda - (\lambda^2-1)^{\frac{1}{2}}}{\lambda + (\lambda^2-1)^{\frac{1}{2}}} \right]}{(\lambda^2-1)^{\frac{3}{2}}}. \quad (16)$$

225 The temporal evolution of the Euler's parameters can be calculated as follows [25]:

$$226 \quad \frac{de_0}{dt} = \frac{1}{2} \left(-e_1\omega_x' - e_2\omega_y' - e_3\omega_z' \right) \quad (17)$$

$$227 \quad \frac{de_1}{dt} = \frac{1}{2} \left(e_0\omega_x' - e_3\omega_y' + e_2\omega_z' \right) \quad (18)$$

$$228 \quad \frac{de_2}{dt} = \frac{1}{2} \left(e_3\omega_x' + e_0\omega_y' - e_1\omega_z' \right) \quad (19)$$

$$229 \quad \frac{de_3}{dt} = \frac{1}{2} \left(-e_2\omega_x' + e_1\omega_y' + e_0\omega_z' \right). \quad (20)$$

230

231 2.4. Computational methodology

232 The solver is developed using OpenFOAM 4.1, an open-sourced CFD platform, hereby referred to
 233 as the NELLI solver [22]. The Euler numerical scheme (transient, first order implicit and bounded) is
 234 used for time derivative terms. The standard finite volume discretization of Gaussian integration with
 235 linear interpolation (with minor modifications) is used for gradient terms, divergence terms and

236 Laplacian terms. Linear interpolation is applied for the interpolation schemes. Surface normal gradient
237 schemes are solved by corrected central differencing schemes. The standard *k-epsilon* model is
238 employed to simulate the flow fields. Coupling between particles and the fluid are achieved through
239 source terms as described in previous work [22]. Particle drag forces are two-way coupled unless
240 otherwise stated, particle torques are only one-way coupled. Particles are initialized and injected into
241 the flow field. The spheroid model is programmed as follows and illustrated in Fig. 1:

- 242 • Fluid velocities at particle locations are interpolated from values of cell centers that are
243 calculated by the Eulerian flow solver.
- 244 • Particle Euler's parameters and transformation matrix are calculated based on particle
245 angular velocities and orientations (i.e. four Euler parameters).
- 246 • Particle drag forces are calculated based on fluid and particle velocities and transformation
247 matrix. As a result, particle velocities are updated.
- 248 • Particle torques are calculated based on fluid velocity gradients and transformation matrix.
249 Particle orientations are updated accordingly.

250

251

Fig. 1

252

253 3. Model verifications and validations

254 The verifications and validations of the spheroid model are divided into two parts (torque and drag)
255 to ensure the correct implantation and the validity of the spheroid model.

256

257 3.1. Torque

258 Investigation of the torque implementation of the spheroid model is conducted by comparing with
259 simulation results obtained from DNS by Zhao et al. [34]. In both simulations, a single spheroidal
260 particle is placed in a simple shear flow in the *xz*-plane where the velocity gradient $\frac{du_x}{dz}$ is set to be 1 s⁻¹
261 ¹. The position of the particle is fixed, but the particle can rotate freely. This configuration is deliberately
262 chosen to avoid additional effects of particle drag force. Other properties of the particle and the flow
263 field are listed in Table 1. Kinematic viscosity of the fluid is arbitrary set to 0.1 m²/s for comparison.

264

265

Table 1

266

267 As the spheroidal particle is not centrally symmetrical, initial orientation of the spheroidal particle
268 can play a role in particle orientation evolutions. Therefore, three different particles that are configured
269 with three different initial orientations are simulated. Their corresponding orientations in the inertial
270 frame are illustrated in Fig. 2. As shown in Fig. 2, the major axes of *Spheroid 1*, *2* and *3* are parallel to
271 the x -, z -, and y -direction of the inertial frame, respectively. It should be noted that the color in Fig. 2 is
272 to make the 3-dimensional particles visually friendly in a 2-dimensional print.

273

274

Fig. 2

275

276 Torque acting on the particle is dependent on fluid strain rate and rotation tensor, which are functions
277 of velocity gradients. Because particle angular velocities are directly coupled to particle torque, the
278 torque of the spheroid model can be verified by investigating the particle angular velocity for different
279 orientations. The temporal evolutions of particle angular velocities in particle frame of *Spheroid 1* and
280 *2* are presented in Fig. 3 (a) and (b), respectively. In Fig. 3, the legend "DNS" represents that simulations
281 are solved by direct numerical simulations (DNS) [34], whereas, the legend "NELLI" refers to that
282 simulations are solved by the spheroid model with the aforementioned in-house solver NELLI [22]. In
283 addition, x , y and z represent the component of the angular velocities in x -, y - and z -direction of particle
284 frame, respectively. In the case of Fig. 3 (a), the major axis of *Spheroid 1* is parallel to the xz -plane
285 where velocity gradient exists, this makes the major axis of spheroidal particle easy to rotate around the
286 y -direction. In addition, since $\frac{du_x}{dz}$ is the only existing velocity gradient, as the spheroidal particle rotates,
287 particle torque reaches its highest value when the spheroidal particle's major axis is parallel to z -
288 direction and lowest when the spheroidal particle's major axis is parallel to x -direction. Therefore, it can
289 be expected that particle angular velocities in x - and z -direction in the particle frame are close to zero,
290 but periodic fluctuations of particle angular velocities of y -direction in particle frame exist. Similar
291 trends can be seen in the case of *Spheroid 2* (Fig. 3 (b)) but showing periodic fluctuations in x -direction.

292 In the case of *Spheroid 3*, the major axis of spheroidal particle is perpendicular to the xz -plane, this
293 makes the particle easy to rotate around the particle major axis at constant speed. As a result, particle
294 angular velocities of x -, y - and z -direction in particle frame remain constant around 0, 0 and 0.5 rad/s,
295 respectively. In all cases, excellent agreement is achieved between results solved by DNS and the solver
296 developed with the spheroid model thereby verifying the correct implementation of the particle torque.

297

298

Fig. 3

299

300 The torque formulas used above are originally developed for an ellipsoid in creeping flows (i.e. Re_p
301 < 1) [32], however the validity of the model in turbulent flow has been proven by Ravik et al. [35]. In
302 their study, DNS simulations were conducted to assess the elongated particle torque under turbulent
303 conditions. Only an approximately four percent root mean square (rms) error associated with Jeffery
304 torques was found under the condition where Stokes number is 1 and ratio of particle length to
305 Kolmogorov scale is 1. They also showed that the error decreases as particle inertia increase, but the
306 error increases exponentially as the ratio of particle length to Kolmogorov scale increases to 8. The error
307 exhibits a plateau trend for particles with even longer length. Therefore, we would assume that it is
308 acceptable to apply these torque formulas into CFD simulations of entrained flow gasification process
309 of pulverized biomass where the flow is turbulent.

310

311 3.2. Drag

312 To verify the implementation of particle drag and fluid-particle two-way coupling, test cases are
313 configured based on the experimental work of Lau et al. [36], in which spherical particles (with less than
314 5% standard deviation) are injected via a jet flow into a wind tunnel. As shown in Fig. 4, a semi-two-
315 dimensional cyclic symmetric $1\text{ m} \times 0.3\text{ m}$ domain (one layer of cell in y -direction) is used to closely
316 mimic the experiment. The circumferential angle is 2° and the nozzle radius is 6.35 mm. The flow and
317 particle properties are listed in Table 2.

318

319

Fig. 4

320
321
322
323
324
325
326
327
328
329
330
331
332
333
334
335
336
337
338
339
340
341
342
343
344
345
346
347

Table 2

The particle loading factor in the experiments is 0.4. It is in the range where interactions among particles can be ignored but interactions between particles and the fluid must be considered. In other words, it is within the regime where two-way coupling should be included in the simulations [36] [37]. The particles in the experiments deviate less than 5% from spherical particles and hence the particles in the simulations are configured as spheroids with aspect ratio of 1.001. Thus particles in both experiments and simulations can be considered spherical, which in turn makes it reasonable to assume particle orientation effects are less pronounced due to the central symmetric characteristics of spheres.

Four simulation cases are carried out. Two of them are solved by employing the sphere model (as described in Section 2.1), whereas the other two are solved by employing the spheroid model (as described in Section 2.2). Normalized centerline velocity profiles (U_c/U_e , U_c is the centerline velocity and U_e is the centerline velocity at the $x/d = 0$) of the particles can be seen in Fig. 5, where simulations using one-way coupling method (a) and two-way coupling method (b) are shown. Additionally, experimental data from Lau et al. [36] is present as well. Due to rapid mixing as the flow develops, particle centerline velocity decreases as x/D_{jet} increases. It can be seen that there are good agreements between the sphere model and the spheroid model in both one-way and two-way coupled cases. This implies that the spheroid model can regress well to the sphere model. However, when comparing simulation results with experimental data, discrepancies are found in the one-way coupled cases while there are better matches in the two-way coupled cases. Normalized particle centerline velocities decay faster in the one-way coupled cases than the two-way couple cases and experiments. Particles have larger inertia than the fluid, hence the particle velocities decay slower than the fluid causing particle velocities to be higher than the fluid velocity in the beginning. In one-way coupled cases, the fluid is not accelerated by the particle. As a result, differences in velocity between the particle and the fluid in one-way coupled cases are larger than for the two-way coupled cases. This leads to larger drag forces acting on particles in the one-way coupled cases, thus causing faster normalized particle centerline velocity decays compared to the two-way coupled cases and the experiments. It can also be observed

348 that there are no major differences when comparing experimental data and two-way coupled simulation
349 results from the sphere model and the spheroid model, thus verifying the implemented particle drag
350 model for spheroids.

351

352

Fig. 5

353

354 The simulation results above also indicate the drag formula is applicable to spherical particles. To
355 further test the validity of the drag formula, simulations are carried out to compare the drag force
356 coefficients from Madhav and Chhabra [38]. In their work, they conducted experiments of needle-
357 shaped steel particle (particle density is 7484 kg/m^3 , aspect ratio ranges from 27.35 to 39.53) free falling
358 in tubes of silicone oil (density is 975 kg/m^3 and dynamic viscosity is $0.97 \text{ Pa}\cdot\text{s}$) and they mapped drag
359 coefficient-Reynolds number relations. We arbitrarily set up particle (with aspect ratio of 33.53)
360 Reynolds numbers in the codes and compare particle drag coefficients calculated by the codes and data
361 from Madhav and Chhabra [38]. The results are shown in Fig. 6, in which the label "Exp." represents
362 experimental data extracted from Madhav and Chhabra [38], whereas, $C_{D,x}$, $C_{D,y}$ and $C_{D,z}$ are simulated
363 particles drag coefficients produced by the spheroid model in the x -, y - and z -direction of particle frame,
364 respectively. There are three drag force coefficients from the current study. This is due to how the
365 spheroid model is implemented in the OpenFOAM platform. As previously mentioned in Section 2.3.1,
366 particle drags are first calculated in the x -, y - and z -direction of particle frame separately, then converted
367 to the format of vectors in the inertia frame. It can be seen from Fig. 6 that the simulated drag coefficients
368 are close to the ones of experiments, thus validating the drag force formulas of the spheroid model. It
369 also can be seen that $C_{D,x}$ and $C_{D,y}$ are the same, but they are different from $C_{D,z}$. This is because that the
370 cross-sectional areas of spheroid particles in the x - and y -direction of particle frame are the same, but
371 they are different from the ones in the z -direction.

372

373

Fig. 6

374

375

376 **4. Application to a simplified entrained flow gasifier**

377 4.1. Simulation setup

378 The validated solver is employed to simulate particle-laden flows in a realistic gasifier configuration.
379 Simonsson et al. [39] reported an atmospheric entrained flow gasifier experiment with stem wood and
380 peat as fuels. A similar but somewhat simplified simulation setup is configured as seen in Fig. 7, where
381 the simulation domain consists of two parts, i.e. a reactor and a burner inlet. The reactor is a cylinder
382 with a length of 1 m and a diameter of 0.5 m. The burner inlet is also in cylinder shape with a length of
383 0.1 m. There are two air registers in the burner inlet. The primary air (orange part in Fig. 7), together
384 with biomass fuels, is transported into the central cylinder tube of 50 mm diameter (hereafter referred
385 as D). The secondary air is introduced via an annular pipe (blue part in Fig. 7, inner diameter 52 mm,
386 outer diameter 56 mm) positioned outside the central tube.

387

388 Fig. 7

389

390 Table 3 summarizes the fluid and particle properties. Operating parameters are set to that of the
391 condition of wood swirl burner operated at equivalence ratio 0.5 [39]. Both swirl and non-swirl
392 conditions are realized by varying the direction of the secondary air, particles are simulated as spherical
393 particles and spheroidal particles with equivalent volume and aspect ratio of 10. In addition, spheroidal
394 particles are injected with three initial orientations as *Spheroid 1*, *2* and *3* as shown in Fig. 2. These three
395 orientations are evenly distributed and each of them makes up one third of the total particle mass flow.
396 Three hexahedral meshes of 224812, 425790 and 748512 cells have been used to test grid independence,
397 respectively. The axial velocities of the fluid (without particles) at the centerline and various axial
398 locations are compared. No significant difference between the latter two meshes is observed, but results
399 from the first mesh are clearly different from the latter two. Therefore, the mesh of 425790 cells (Fig.
400 8) is employed for further simulations. The time step for the simulation is 5×10^{-5} s. This work also uses
401 “StochasticDispersionRAS” model from OpenFOAM 4.x for turbulent dispersion simulation, the model
402 creates velocity perturbation randomly based on kinetic energy of turbulence and its general theory can
403 be found in [40].

404

405

Table 3

406

407

Fig. 8

408

409 4.2. Results and discussions

410 In this subsection, simulation results are presented in the form of axial, radial, and tangential
411 profiles at different axial locations, z/D , along the flow. Here, D refers to the diameter of inner tube,
412 whereas r and τ refer to radial and tangential coordinates, respectively. The results calculated from
413 different approaches under both swirl and non-swirl conditions are compared. Particle results presented
414 below are sampled over 50 time steps to ensure there are sufficient number of particles so that results
415 are statistically independent.

416

417 4.2.1. Axial velocity profile

418 Figure 9 shows axial velocities of fluid and particles velocity along the reactor radius at different
419 axial locations. In terms of fluid velocities in both swirl and non-swirl conditions, at the axial location
420 of $z/D = 0$, the peaks of axial velocities can be observed around radial location of $r/D = 0.52-0.56$ where
421 secondary air is injected. The axial location of $z/D = 0$ is where primary air and secondary air enter the
422 reactor from their respective tubes. As the flow develops further downstream, primary air and secondary
423 air start to mix. At axial location of $z/D = 5$, the locations of the peak of fluid axial velocity under both
424 swirl conditions move closer to the center in radial directions, instead of remaining around the radial
425 location where secondary air is injected. The peaks disappear further downstream and overall axial
426 velocities decrease at axial locations $z/D = 10$ and 15 , where effects of secondary are much less
427 prominent and the fluid momentum decays due to rapid mixing of primary air and secondary air.

428 Particles are injected with the exact same velocity as the primary air at the inlet ($z/D = -0.2$).
429 Regardless of swirling conditions, particle axial velocities at the axial location of $z/D = 0$ only differs
430 slightly from the fluid velocity in the radial region where r/D is less than 0.5 . Particles, which have the
431 same initial velocity as primary air, first accelerate ($z/D = 5$) and then slow down ($z/D = 10$ and 15)

432 from upstream to downstream. It shows particles preserve similar trends when comparing to the fluid
433 profiles, but with a time delay. This is expected as particles here have larger inertia than the fluid. When
434 studying the differences at different swirling conditions, it can be observed that particles are distributed
435 over a wider range of radial locations in swirl conditions than non-swirl conditions, due to the swirl of
436 the fluid as will be further explained in Section 4.2.2.

437

438

Fig. 9

439

440 When comparing between the sphere model and the spheroid model, it can be seen from Fig. 9 that
441 the spherical particles have a much narrower axial velocity distributions than the spheroidal particles,
442 regardless of swirling conditions. The axial velocities of spherical particles concentrate in a narrow
443 region and this pattern continues from upstream to downstream. However, the axial velocities of
444 spheroidal particles become more divergent when they come downstream. A possible cause of such
445 differences between spherical and spheroidal particles could come from initial orientations of spheroidal
446 particle. Figure 10 presents a more detailed overview of particle axial velocities at axial location of z/D
447 = 15. For the simplicity, only the non-swirl conditions are shown. Particles of *Spheroid 1* and *Spheroid*
448 *3* have similar distribution patterns for axial velocity, ranging from 3 to 7 /s, whereas particles of *Sphere*
449 and *Spheroid 2* are narrowly distributed around 5 and 6 m/s, respectively. The major axes of *Spheroid*
450 *1* and *3* are perpendicular to the reactor axial direction, but is parallel in the case of *Spheroid 2*. Since
451 large gradients of fluid axial velocity exist in radial directions due to the configuration of inlet conditions,
452 particles of *Spheroid 1* and *Spheroid 3* are much easier to rotate than particles of *Spheroid 2*. As a result,
453 the cross-sectional area of a *Spheroid 2* particle projected to the flow direction does not vary significantly
454 from one particle to another and little differences between particle axial velocities and drag forces exist
455 among particles of *Spheroid 2*.

456

457 Differences of averaged axial velocities of particles predicted by these three models can be observed
458 from upstream to downstream. One factor that contributes to such differences could be how different
459 models calculate particle projected cross-sectional areas to the flow when simulating particle drag forces.
The sphere model treats pulverized biomass particles as spheres of equivalent volumes, this means the

460 particle projected cross-sectional areas to the flow remain constant. The simplified non-sphere model
461 use sphericity to compensate particle shape irregularities and thus making particle projected cross-
462 sectional areas to the flow being different than the ones calculated by the sphere model. Although the
463 simplified non-sphere model considers particles being non-spherical, the sphericity of a particle still
464 remains constant as long as the shape of the particle does not change. This indicates particles of different
465 orientations will have the same drag forces if other conditions are the same, which is not the case in
466 reality. The spheroid model takes one step further by considering particle orientations by calculating
467 particle torques and then modify particle drag forces. In this way, particles of different orientations will
468 have different drag forces when other conditions are the same. Furthermore, values of standard
469 derivation indicate how scattered or dispersed particles are. The different ways modelling particles could
470 also explain why the standard derivations of particle axial velocities predicted by the sphere model and
471 the simplified non-sphere model are in closer agreement than the spheroid model as clearly seen in Fig
472 9. Particles predicted by the spheroid model are more scattered from the other two models since the
473 spheroid model considers particle orientations and one particle may have very different temporal
474 development of orientations than another particle.

475

476

Fig. 10

477

478 The particle axial velocity is closely connected to particle residence time. In theory, particle residence
479 time, t , over a certain distance, L , is dependent on particle velocity development along the distance, $U(L)$.
480 This can be expressed by

481

$$t = \int \frac{dL}{U(L)} \quad (21)$$

482

483

484

485

486

Therefore, a higher axial velocity predicts a shorter residence time if other conditions are the same. Particle ages along the reactor radius at different axial locations and swirling conditions are shown in Fig. 11. Particle age refers to the time it takes for a particle to reach the position of the measurement from the inlet, thus can be used as an indicator for particle residence time. From upstream to downstream, particle age variations become bigger under both swirl and non-swirl conditions. This phenomenon is

487 especially pronounced for spheroidal particles under swirl conditions. Given the same axial location,
488 particle ages, due to the differences of axial velocities, are also different along radial directions. It can
489 also be seen that particle ages vary more in the spheroid model than the sphere model, especially in swirl
490 cases. This is in agreement with patterns observed on particle axial velocities.

491

492 Fig. 11

493

494 4.2.2. Radial and tangential velocity profiles

495

496 Fig. 12

497

498 Figure 12 shows the particle and fluid radial velocity distribution along the reactor radius. The radial
499 velocity, U_r , is defined as the velocity component that is perpendicular to axial direction and parallel to
500 radial direction. In non-swirl cases, fluid radial velocities at axial location of $z/D = 0$ peak around the
501 radial location where secondary air is injected. This is due to the mixing of primary air and secondary
502 air in radial direction. Since the fluid has higher radial velocity than the particles, they are accelerated
503 by the fluid in the radial direction. As the flow develops further downstream, fluid radial velocity decays
504 rapidly due to fast mixing and remains small. However, particles have much higher inertia than fluid so
505 their radial velocities still increase. When there are swirls in the flow field, despite the fact that the fluid
506 has very similar radial velocity profile as in the non-swirl cases, particle radial velocities are different
507 from non-swirl cases. At axial location of $z/D = 5$, particle radial velocities increase along the radius in
508 the swirl cases whereas in the non-swirl cases velocities do not increase significant along the radius.
509 When there are swirls in the flow fields, particles have tangential velocities because of the swirling of
510 fluids. This creates the possibility for particles to have higher radial velocities. Particles must have
511 enough centripetal forces to keep circular motions at certain radius, otherwise, particles have centrifugal
512 motion, thus resulting velocities and displacements in radial directions. This is confirmed in Fig. 13,
513 where the particle and fluid tangential velocity distribution along reactor radius is presented. Tangential
514 velocity, U_τ , is defined as the velocity component that is perpendicular to axial direction and radial

515 direction. In Fig. 13, when there is no swirl, from upstream to downstream, fluid tangential velocity
516 remains very small, particle tangential velocities on the other hand first start at 0 m/s then become
517 dispersed to a range of ± 0.5 m/s. One possible cause for this could be the fact that dispersion model is
518 applied in all simulations. The model creates velocity perturbation randomly, which gives particle
519 tangential velocities. In swirl cases, fluid tangential velocities can clearly be observed. In the upstream
520 of $z/D = 0$, fluids have the highest tangential velocities at the location where secondary air is injected
521 into the reactor, as the flow develops to axial locations of $z/D = 5, 10$ and 15 , fluid tangential velocities
522 decay due to rapid mixing of primary and secondary air. Particles tangential velocities, on the other hand,
523 remain concentrated around the vicinity of 0 m/s at the axial location of $z/D = 0$, then becomes
524 accelerated by the fluid at $z/D = 5$, then decay further downstream at $z/D = 10$ and 15 . The slower
525 tangential velocity decays for particles compared to the fluid can be explained by the fact that particles
526 have larger inertia than fluids. Regardless of swirl conditions, the spheroid model predicts larger
527 standard deviations of radial and tangential velocities than the other two models. This trend is similar to
528 what is observed in axial velocity profiles and could be explained in a similar way as stated in Section
529 4.2.1.

530

531

Fig. 13

532

533 Figure 14 shows particle concentrations at swirl conditions using the classical sphere model and the
534 implemented spheroid model. A cross-sectional space of $z/D = \pm 0.05$ in axial direction is sampled at
535 $z/D = 5, 10$ and 15 , respectively. Then each cross-sectional space is evenly divided into 50×50 unit
536 spaces in the xy -plane. The color bar indicates the local concentration of particle i.e. number of particles
537 per unit space. In the upstream region ($z/D = 5$), both the sphere model and spheroid model give very
538 similar results that particles are concentrated in the center. As the particles develop with the flow to
539 further downstream, particles spread out. Many particles can be still observed around the center in the
540 simulation using the sphere model further downstream ($z/D = 15$), whereas a more evenly distributed
541 particle profile can be found in the results using spheroid model. This is in agreement with the

542 aforementioned expectation that spheroidal particles are more dispersed and thus locally less
543 concentrated.

544

545 Fig. 14

546

547 4.2.3. Expected implications of model for non-spherical under reactive conditions

548 The observed phenomena in the cold flow simulation has also implications for the CFD simulations
549 of biomass conversion using Eulerian-Lagrangian method. For example, when simulating the entrained
550 flow gasification of biomass, where swirl conditions are typically expected, there can be significant
551 differences between simulations using the sphere assumption and the spheroid assumption. Spheroidal
552 particles have larger surface areas than spherical particles of the same volume. This makes heating up
553 spheroidal particles easier than spherical particles in the same environment. A faster heating process
554 could prompt the conversion of biomass particles, especially the endothermic drying process, and
555 consequently using a spherical model approach may underestimate this. Furthermore, in an entrained
556 flow gasifier, some volatile gases released from the fuel reacting with oxygen to provide heat for the
557 gasification reactions. Reactants must be mixed on a microscale level and be present in the reactive
558 mixture for a certain period of time in order to undergo thermal conversion [23]. In other words, local
559 species concentrations and residence times are determining factors of the chemical reactions. As found
560 in the cold flow simulation, spheroidal particles are clearly more dispersed than spherical particles under
561 swirl conditions. Simulations using the spherical particle model may underpredict the mixing of volatile
562 gases and oxygen, thus presumably leading to a slower combustion of volatile gases. Apart from gas
563 phase reactions, the choice of sphere or spheroid model also affects gas-solid phase reactions. The
564 traditional spherical particle model may produce more concentrated char clusters and thus resulting a
565 slower conversion process. Similar analysis can also be conducted for the simplified non-sphere model,
566 as it predicts less scattered results in terms of particle velocities when compared to the spheroid model.
567 However, it should be noted that in the later stage of the entrained flow gasification of biomass, as
568 biomass particles react and convert, shapes of biomass particles become more and more spherical as
569 evidenced in [5]. Particle size changes can affect the particle aspect ratio. It also may influence

570 pulverized biomass particle size distribution in the flame as this is the case for coal [41]. Nevertheless,
571 the overall implications of replacing spherical particle models with spheroid particle models are in need
572 for further studies under reactive conditions, which is the next step of our research.

573

574 **5. Conclusions**

575 This work presents a detailed implementation of the spheroid particle model for simulating
576 pulverized biomass particle. The spheroid particle model is implemented into an Euler-Lagrange CFD
577 solver in OpenFOAM and is verified and validated against DNS and experiments. Non-reactive test
578 cases are executed to predict particle behaviors in a configuration similar to an entrained flow gasifier.
579 When comparing to simulations by using the sphere model and the simplified non-sphere model, the
580 spheroid model shows different results in terms of particle axial, radial and tangential velocities. Larger
581 standard deviations of particle velocities are also observed in the case of the spheroid model. This could
582 be caused by the fact that the spheroid model takes particle orientations into account while the other two
583 models do not. Moreover, under swirling conditions, the spheroid model gives more diverse particle
584 concentrations and residence times than the traditional sphere model. All the above indicates that using
585 the spheroid model could have major influences on reactive simulation and this should be further
586 investigated.

587

588 **Acknowledgement**

589 This work is a part of the GAFT project (Gasification and FT-Synthesis of Lignocellulosic
590 Feedstocks; project number: 244069) and is also in partnership with Sino-Norwegian Partnership on
591 Sustainable Energy (project number: 250146). Both of them are co-funded the Research Council of
592 Norway and industrial partners. In addition, L. Zhao thanks the support of Nature Science Foundation
593 of China through Grant No. 11702158, 91752205 and 11490551.

594 The authors would also like to express gratitude to Professor Helge I. Andersson for helping
595 implement particle torque. We would also like to thank Mr. Fredrik Grøvdal for his mathematical
596 support about spheroid sphericities. In addition, we acknowledge Dr. Niranjan Reddy Challabotla for
597 his help in understanding torques of spheroid. At the time when this paper is written, all of the three
598 researchers are affiliated with Department of Energy and Process Engineering, Norwegian University
599 of Science and Technology, Norway.

600

601 **Nomenclature**

Notation	Description
A	transformation matrix
a	spheroid minor axis [m]
B_1, B_2, B_3, B_4	model coefficient based on particle sphericity
C_D	drag force coefficient
c	spheroid major axis [m]
D	central tube diameter in model application [m]
D_{jet}	jet diameter in drag model verification [m]
D_p	particle diameter [m]
d_{ij}	deformation rate [s^{-1}]
e_0, e_1, e_2, e_3	Euler parameters
F_D	particle drag force [N]
I	particle moment of inertia [$kg \cdot m^2$]
i, j, k	tensor notation indices

m_p	particle mass [kg]
N	particle torque [N·m]
Re_p	particle Reynolds number
r	radial coordinates [m]
t	time [s]
U_c	centerline velocity [m/s]
U_e	jet exit velocity [m/s]
U_f	fluid velocity [m/s]
U_p	particle velocity [m/s]
U_r	radial velocity [m/s]
U_z	axial velocity [m/s]
U_τ	tangential velocity [m/s]
w_{ij}	spin tensor [s ⁻¹]
\mathbf{x}	inertial frame
\mathbf{x}' or $'$	particle frame
\mathbf{x}'' or $''$	co-moving frame
x, y, z	coordinates in x -, y -, z -direction, respectively [m]
$\alpha_0, \beta_0, \gamma_0$	dimensionless parameters
λ	particle aspect ratio
μ_f	fluid dynamic viscosity [N·s/m ²]
ν_f	fluid kinematic viscosity [m ² /s]
ρ_f	fluid density [kg/m ³]
ϕ	sphericity
ϕ_{\parallel}	lengthwise sphericity
ϕ_{\perp}	crosswise sphericity
ω	angular velocity

602

603 **References**

- 604 [1] Ari I, Sari R. Differentiation of developed and developing countries for the Paris Agreement.
605 *Energy Strateg Rev* 2017;18:175–82. doi:10.1016/j.esr.2017.09.016.

- 606 [2] Zwart RWR, Boerrigter H, van der Drift A. The impact of biomass pretreatment on the
607 feasibility of overseas biomass conversion to Fischer-Tropsch products. *Energy and Fuels*
608 2006;20:2192–7. doi:10.1021/ef060089f.
- 609 [3] Li T, Wang L, Ku X, Güell BM, Løvås T, Shaddix CR. Experimental and modeling study of
610 the effect of torrefaction on the rapid devolatilization of biomass. *Energy and Fuels* 2015.
611 doi:10.1021/acs.energyfuels.5b00348.
- 612 [4] Gubba SR, Ma L, Pourkashanian M, Williams A. Influence of particle shape and internal
613 thermal gradients of biomass particles on pulverised coal/biomass co-fired flames. *Fuel Process*
614 *Technol* 2011;92:2185–95. doi:10.1016/j.fuproc.2011.07.003.
- 615 [5] Panahi A, Levendis YA, Vorobiev N, Schiemann M. Direct observations on the combustion
616 characteristics of Miscanthus and Beechwood biomass including fusion and spherodization.
617 *Fuel Process Technol* 2017;166:41–9. doi:10.1016/j.fuproc.2017.05.029.
- 618 [6] Gao X, Zhang Y, Li B, Yu X. Model development for biomass gasification in an entrained flow
619 gasifier using intrinsic reaction rate submodel. *Energy Convers Manag* 2016;108:120–31.
620 doi:10.1016/j.enconman.2015.10.070.
- 621 [7] Ku X, Jin H, Lin J. Comparison of gasification performances between raw and torrefied
622 biomasses in an air-blown fluidized-bed gasifier. *Chem Eng Sci* 2017;168:235–49.
623 doi:10.1016/j.ces.2017.04.050.
- 624 [8] Simone M, Biagini E, Galletti C, Tognotti L. Evaluation of global biomass devolatilization
625 kinetics in a drop tube reactor with CFD aided experiments. *Fuel* 2009;88:1818–27.
626 doi:10.1016/j.fuel.2009.04.032.
- 627 [9] Zhang W, Tainaka K, Ahn S, Watanabe H, Kitagawa T. Experimental and numerical
628 investigation of effects of particle shape and size distribution on particles' dispersion in a
629 coaxial jet flow. *Adv Powder Technol* 2018. doi:10.1016/j.appt.2018.06.008.
- 630 [10] van Wachem B, Zastawny M, Zhao F, Mallouppas G. Modelling of gas-solid turbulent channel
631 flow with non-spherical particles with large Stokes numbers. *Int J Multiphase Flow* 2015;68:80–
632 92. doi:10.1016/j.ijmultiphaseflow.2014.10.006.
- 633 [11] Haider A, Levenspiel O. Drag coefficient and terminal velocity of spherical and nonspherical

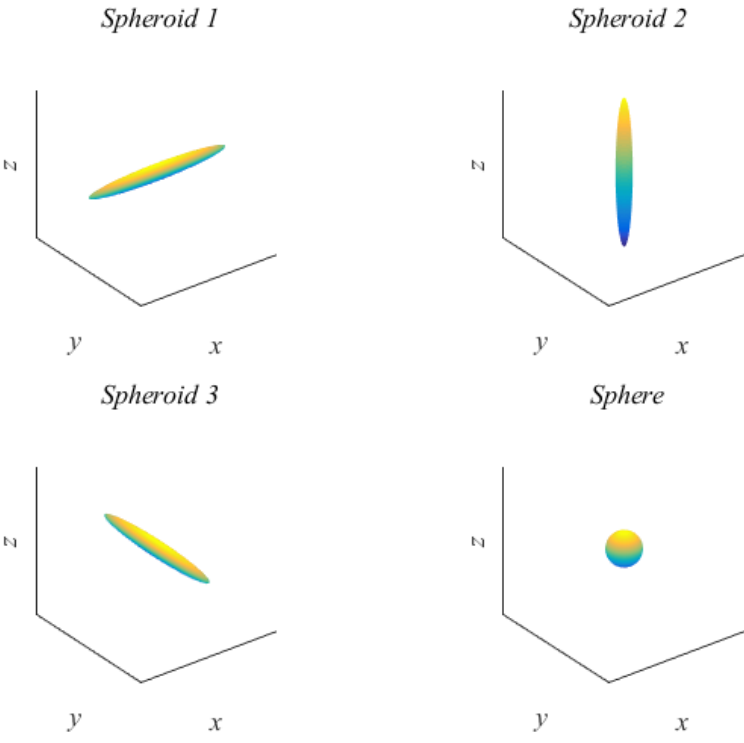
- 634 particles. *Powder Technol* 1989;58:63–70. doi:10.1016/0032-5910(89)80008-7.
- 635 [12] Ma L, Jones JM, Pourkashanian M, Williams A. Modelling the combustion of pulverized
636 biomass in an industrial combustion test furnace. *Fuel* 2007;86:1959–65.
637 doi:10.1016/j.fuel.2006.12.019.
- 638 [13] Backreedy RI, Fletcher LM, Jones JM, Ma L, Pourkashanian M, Williams A. Co-firing
639 pulverised coal and biomass: A modeling approach. *Proc Combust Inst* 2005;30 II:2955–64.
640 doi:10.1016/j.proci.2004.08.085.
- 641 [14] Rosendahl L. Using a multi-parameter particle shape description to predict the motion of non-
642 spherical particle shapes in swirling flow. *Appl Math Model* 2000;24:11–25.
643 doi:10.1016/S0307-904X(99)00023-2.
- 644 [15] Hölzer A, Sommerfeld M. New simple correlation formula for the drag coefficient of non-
645 spherical particles. vol. 184. 2008. doi:10.1016/j.powtec.2007.08.021.
- 646 [16] Schiemann M, Haarmann S, Vorobiev N. Char burning kinetics from imaging pyrometry:
647 Particle shape effects. *Fuel* 2014;134:53–62. doi:10.1016/j.fuel.2014.05.049.
- 648 [17] Vorobiev N, Becker A, Kruggel-Emden H, Panahi A, Levendis YA, Schiemann M. Particle
649 shape and Stefan flow effects on the burning rate of torrefied biomass. *Fuel* 2017;210:107–20.
650 doi:10.1016/j.fuel.2017.08.037.
- 651 [18] Grow DT. Mass and heat transfer to an ellipsoidal particle. *Combust Flame* 1990;80:209–13.
652 doi:10.1016/0010-2180(90)90128-E.
- 653 [19] Li J, Zhang J. Analytical study on char combustion of spheroidal particles under forced
654 convection. *Powder Technol* 2017;313:210–7. doi:10.1016/j.powtec.2017.02.054.
- 655 [20] The OpenFOAM Foundation. OpenFOAM n.d. <https://openfoam.org> (accessed May 25, 2018).
- 656 [21] Ku X, Li T, Løvås T. Influence of drag force correlations on periodic fluidization behavior in
657 Eulerian–Lagrangian simulation of a bubbling fluidized bed. *Chem Eng Sci* 2013;95:94–106.
658 doi:10.1016/j.ces.2013.03.038.
- 659 [22] Ku X, Li T, Løvås T. Eulerian–Lagrangian Simulation of Biomass Gasification Behavior in a
660 High-Temperature Entrained-Flow Reactor. *Energy & Fuels* 2014;28:5184–96.
661 doi:10.1021/ef5010557.

- 662 [23] Andersson B, Andersson R, Håkansson L, Mortensen M, Sudiyo R, Van Wachem B.
663 Computational fluid dynamics for engineers. 2011. doi:10.1017/CBO9781139093590.
- 664 [24] Liu AB, Mather D, Reitz RD. Modeling the Effects of Drop Drag and Breakup on Fuel Sprays.
665 SAE Int Congr Expo 1993;298:1–6. doi:10.4271/93007.
- 666 [25] Marchioli C, Fantoni M, Soldati A. Orientation, distribution, and deposition of elongated,
667 inertial fibers in turbulent channel flow. *Phys Fluids* 2010;22:033301. doi:10.1063/1.3328874.
- 668 [26] Mortensen PH, Andersson HI, Gillissen JJJ, Boersma BJ. Dynamics of prolate ellipsoidal
669 particles in a turbulent channel flow. *Phys Fluids* 2008;20:093302. doi:10.1063/1.2975209.
- 670 [27] Zhang H, Ahmadi G, Fan F-G, McLaughlin JB. Ellipsoidal particles transport and deposition in
671 turbulent channel flows. *Int J Multiph Flow* 2001;27:971–1009. doi:10.1016/S0301-
672 9322(00)00064-1.
- 673 [28] Spring KW. Euler parameters and the use of quaternion algebra in the manipulation of finite
674 rotations: A review. *Mech Mach Theory* 1986;21:365–73. doi:10.1016/0094-114X(86)90084-
675 4.
- 676 [29] Morton HS, Junkins JL, Blanton JN. Analytical solutions for Euler parameters. *Celest Mech*
677 1974;10:287–301. doi:10.1007/BF01586859.
- 678 [30] Mandø M, Rosendahl L. On the motion of non-spherical particles at high Reynolds number.
679 *Powder Technol* 2010;202:1–13. doi:10.1016/j.powtec.2010.05.001.
- 680 [31] Jeffery GB. The Motion of Ellipsoidal Particles Immersed in a Viscous Fluid. *Proc R Soc A*
681 *Math Phys Eng Sci* 1922;102:161–79. doi:10.1098/rspa.1922.0078.
- 682 [32] Andersson HI, Zhao L, Barri M. Torque-coupling and particle–turbulence interactions. *J Fluid*
683 *Mech* 2012;696:319–29. doi:10.1017/jfm.2012.44.
- 684 [33] Gallily I, Cohen AH. On the orderly nature of the motion of nonspherical aerosol particles. II.
685 Inertial collision between a spherical large droplet and an axially symmetrical elongated
686 particle. *J Colloid Interface Sci* 1979. doi:10.1016/0021-9797(79)90287-X.
- 687 [34] Zhao L, Andersson HI. Why spheroids orient preferentially in near-wall turbulence. *J Fluid*
688 *Mech* 2016;807:221–34. doi:10.1017/jfm.2016.619.
- 689 [35] Ravnik J, Marchioli C, Soldati A. Application limits of Jeffery's theory for elongated particle

- 690 torques in turbulence: a DNS assessment. *Acta Mech* 2018. doi:10.1007/s00707-017-2002-5.
- 691 [36] Lau TCW, Nathan GJ. Influence of Stokes number on the velocity and concentration
692 distributions in particle-laden jets. *J Fluid Mech* 2014. doi:10.1017/jfm.2014.496.
- 693 [37] Elgobashi S. An Updated Classification Map of Particle-Laden Turbulent Flows. In:
694 Balachandar S, Prosperetti A, editors. *IUTAM Symp. Comput. Approaches to Multiph. Flow*,
695 Dordrecht: Springer Netherlands; 2006, p. 3–10. doi:10.1007/1-4020-4977-3_1.
- 696 [38] Madhav GV, Chhabra RP. Drag on non-spherical particles in viscous fluids. *Int J Miner*
697 *Process* 1995;43:15–29. doi:10.1016/0301-7516(94)00038-2.
- 698 [39] Simonsson J, Bladh H, Gullberg M, Pettersson E, Sepman A, Ögren Y, et al. Soot
699 Concentrations in an Atmospheric Entrained Flow Gasifier with Variations in Fuel and Burner
700 Configuration Studied Using Diode-Laser Extinction Measurements. *Energy and Fuels*
701 2016;30:2174–86. doi:10.1021/acs.energyfuels.5b02561.
- 702 [40] Gosman AD, Ioannides E. Aspects of Computer Simulation of Liquid-Fueled Combustors. *J*
703 *Energy* 1983. doi:10.2514/3.62687.
- 704 [41] Muto M, Tanno K, Kurose R. A DNS study on effect of coal particle swelling due to
705 devolatilization on pulverized coal jet flame. *Fuel* 2016;184:749–52.
706 doi:10.1016/j.fuel.2016.07.070.
- 707 [42] Lundell F, Carlsson A. Heavy ellipsoids in creeping shear flow: Transitions of the particle
708 rotation rate and orbit shape. *Phys Rev E - Stat Nonlinear, Soft Matter Phys* 2010;81.
- 709 [43] Jebakumar AS, Abraham J. Comparison of the structure of computed and measured particle-
710 laden jets for a wide range of Stokes numbers. *Int J Heat Mass Transf* 2016;97:779–86.
711 doi:10.1016/j.ijheatmasstransfer.2016.02.074.

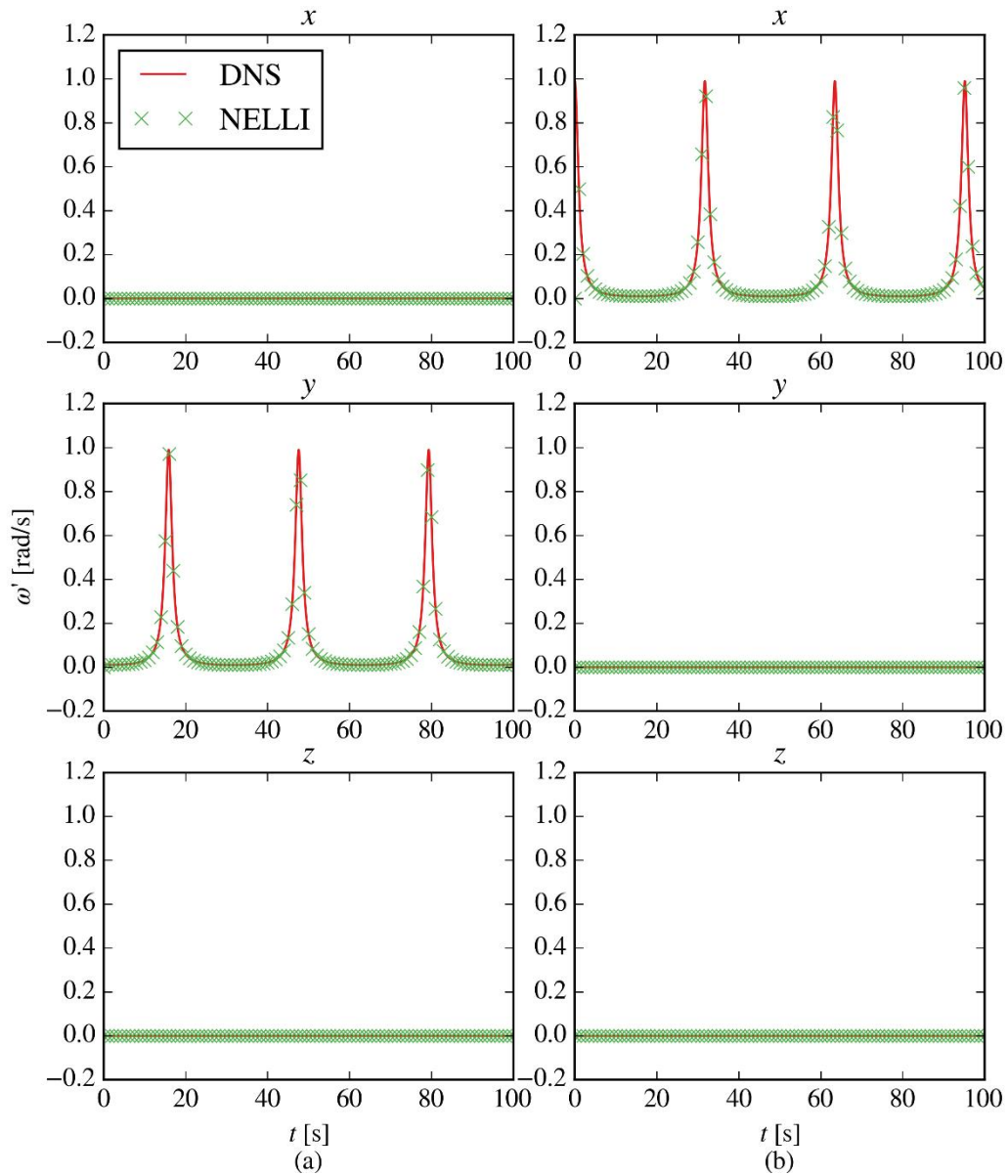
712

713



717
718
719

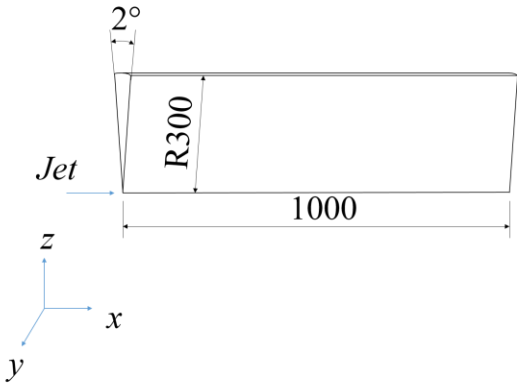
Fig. 2 Initial orientations of particle in inertial frame



720

721 Fig. 3 Angular velocity profile of (a) *Spheroid 1* and (b) *Spheroid 2*. “DNS” and “NELLI”
 722 represent simulations are solved by the DNS [34] and the spheroid model with the aforementioned in-
 723 house solver NELLI [22], respectively; x , y and z represent the component of the angular velocities in
 724 x -, y - and z -direction of particle frame, respectively.

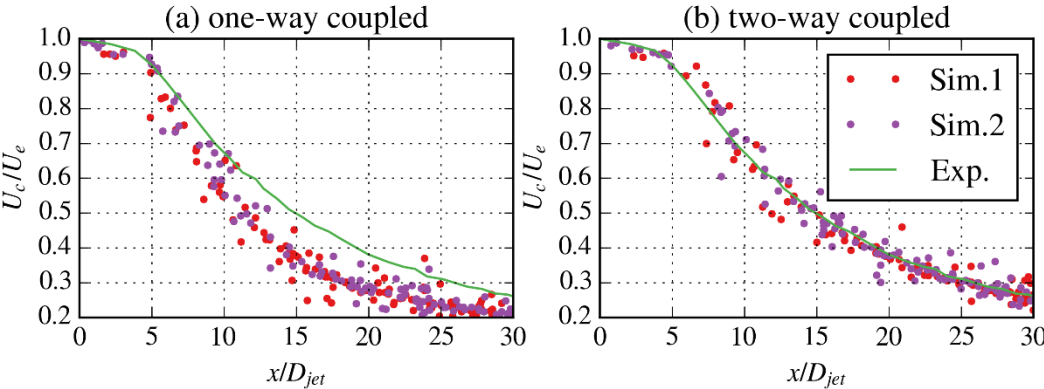
725



726

727 Fig. 4 Simulation domain of the particle-laden jet (unit: mm). The length of the domain is 1000mm
728 and the radius is 300mm. Nozzle radius is 6.35 mm.

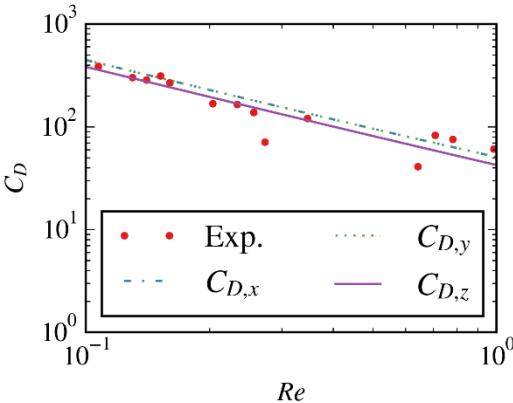
729



730

731 Fig. 5 Particle centerline velocity profile for one-way coupling (left) and two-way coupling (right).
732 "Sim.1" and "Sim.2" stand for simlautions employing spheres and spheroids with aspect ratio close to
733 1 respectively, "Exp." represents experiments.

734



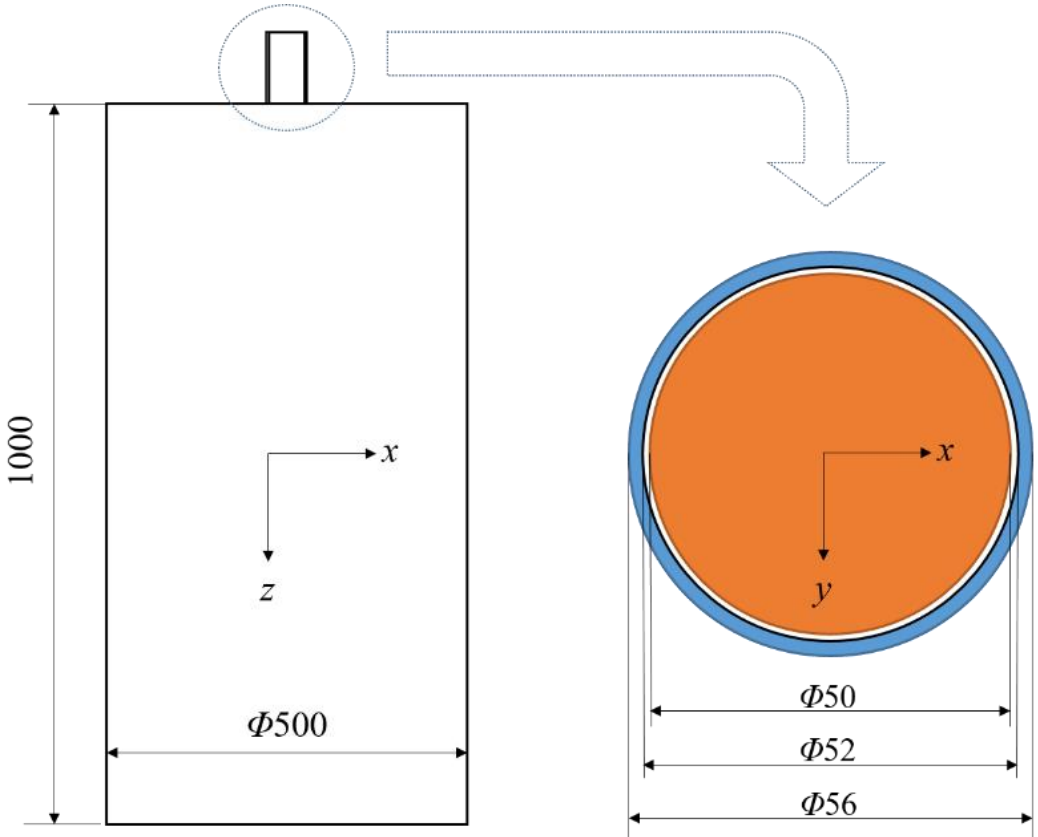
735

736

737

738

Fig. 6 Calculated drag coefficients for the three spatial directions compared to experimentally obtained drag force coefficient as function of Reynolds numbers.



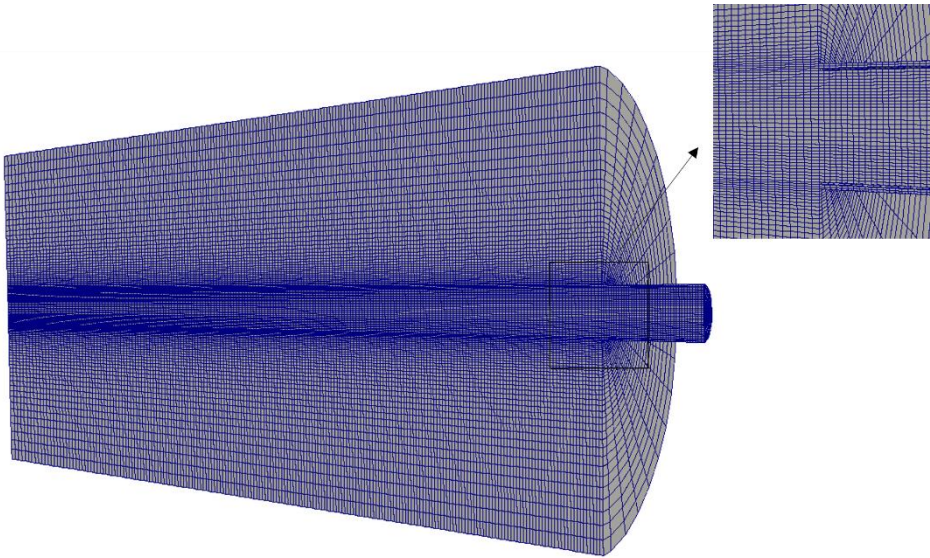
739

740

741

742

Fig. 7 Simulation domain of a simplified entrained flow reactor (Left: front view of the whole domain; right: inlet. Unit: mm)

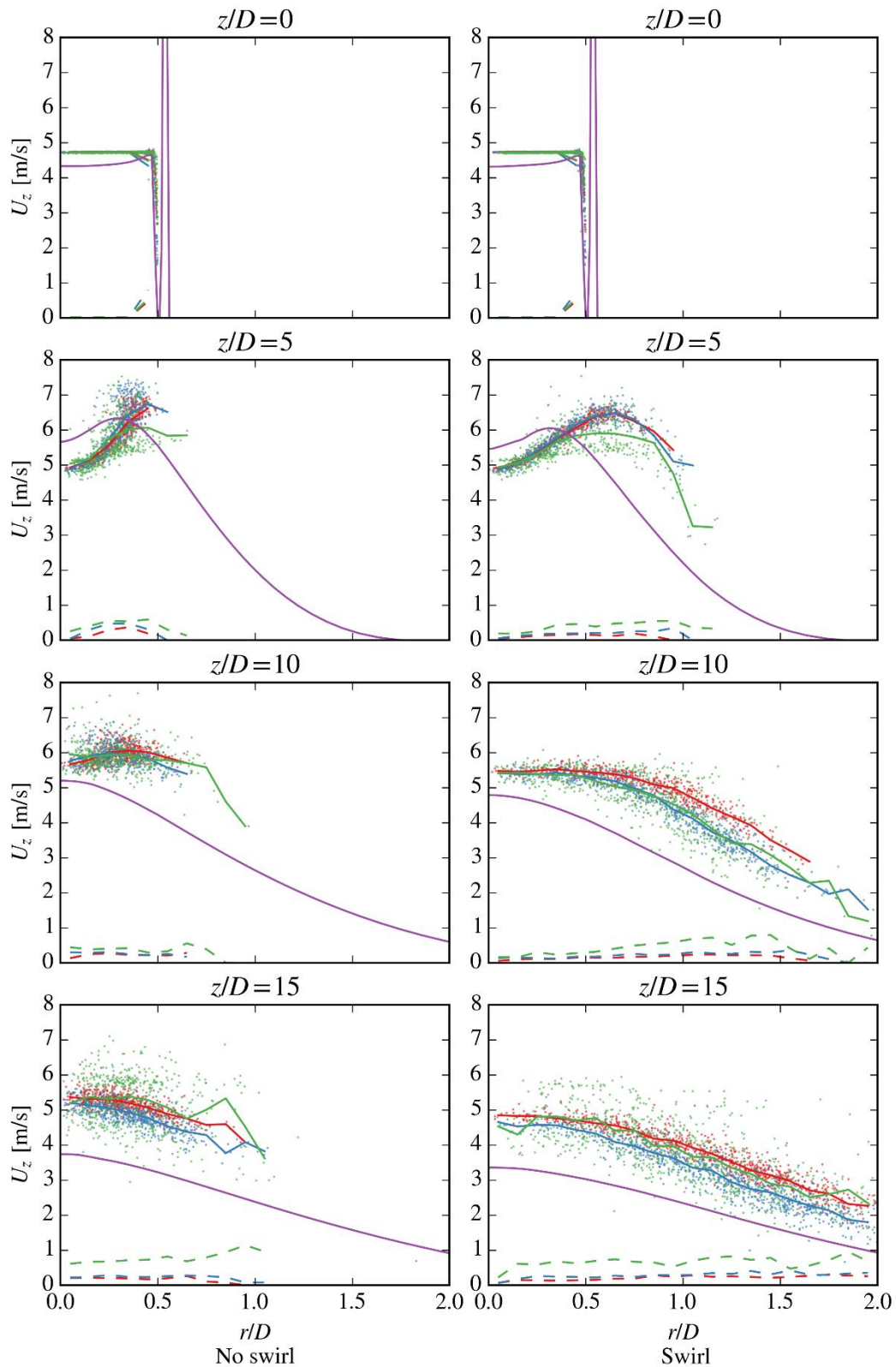


743

744

Fig. 8 Mesh of the simplified entrained flow gasifier

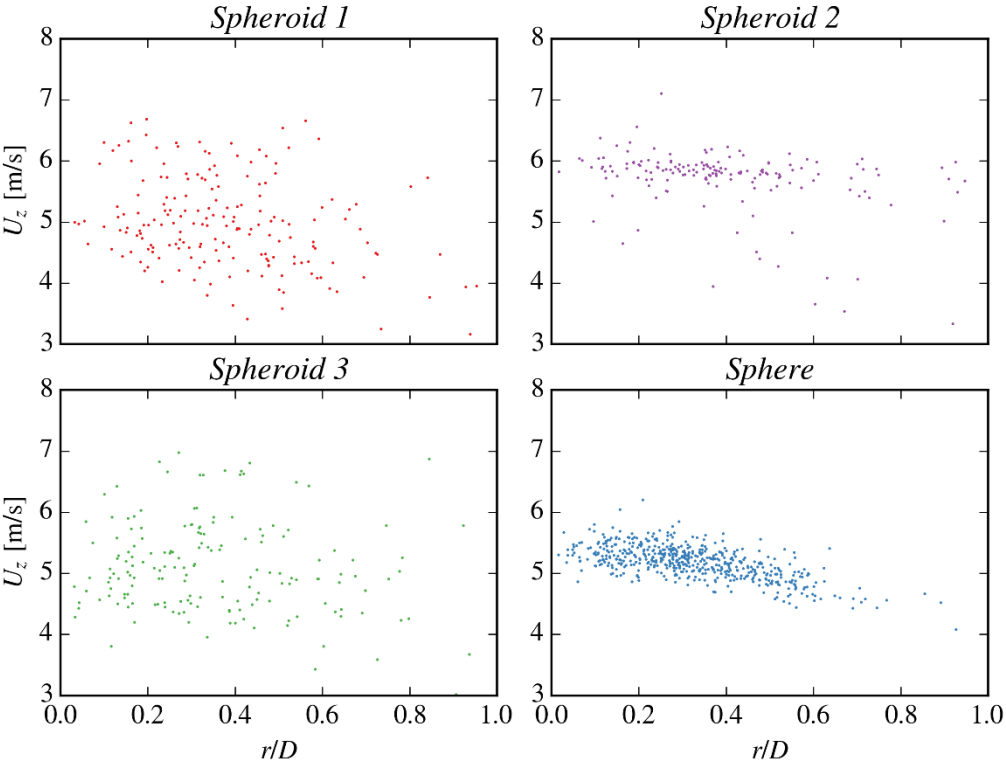
745



746

747 Fig. 9 Particle and fluid axial velocity distribution along reactor radius at different heights along the
 748 reactor (vertical) for non-swirl and swirl conditions (horizontal). Solid line: fluid or averaged particle
 749 velocity; dash line: standard deviation of particle velocity; scatter: particle velocity. Purple: fluid; red:
 750 the sphere model; blue: the simplified non-sphere model; green: the spheroid model.

751



752

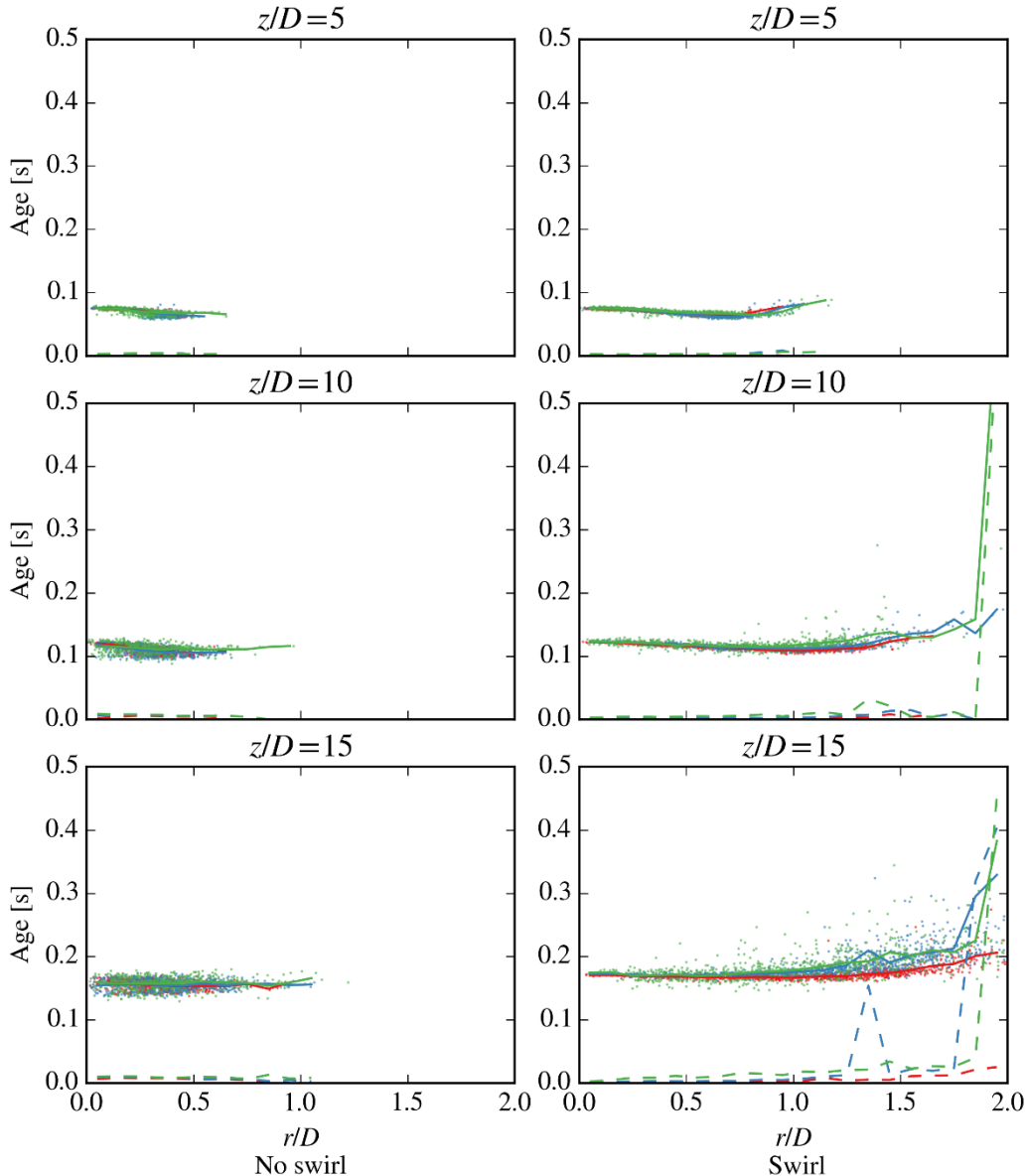
753

754

755

756

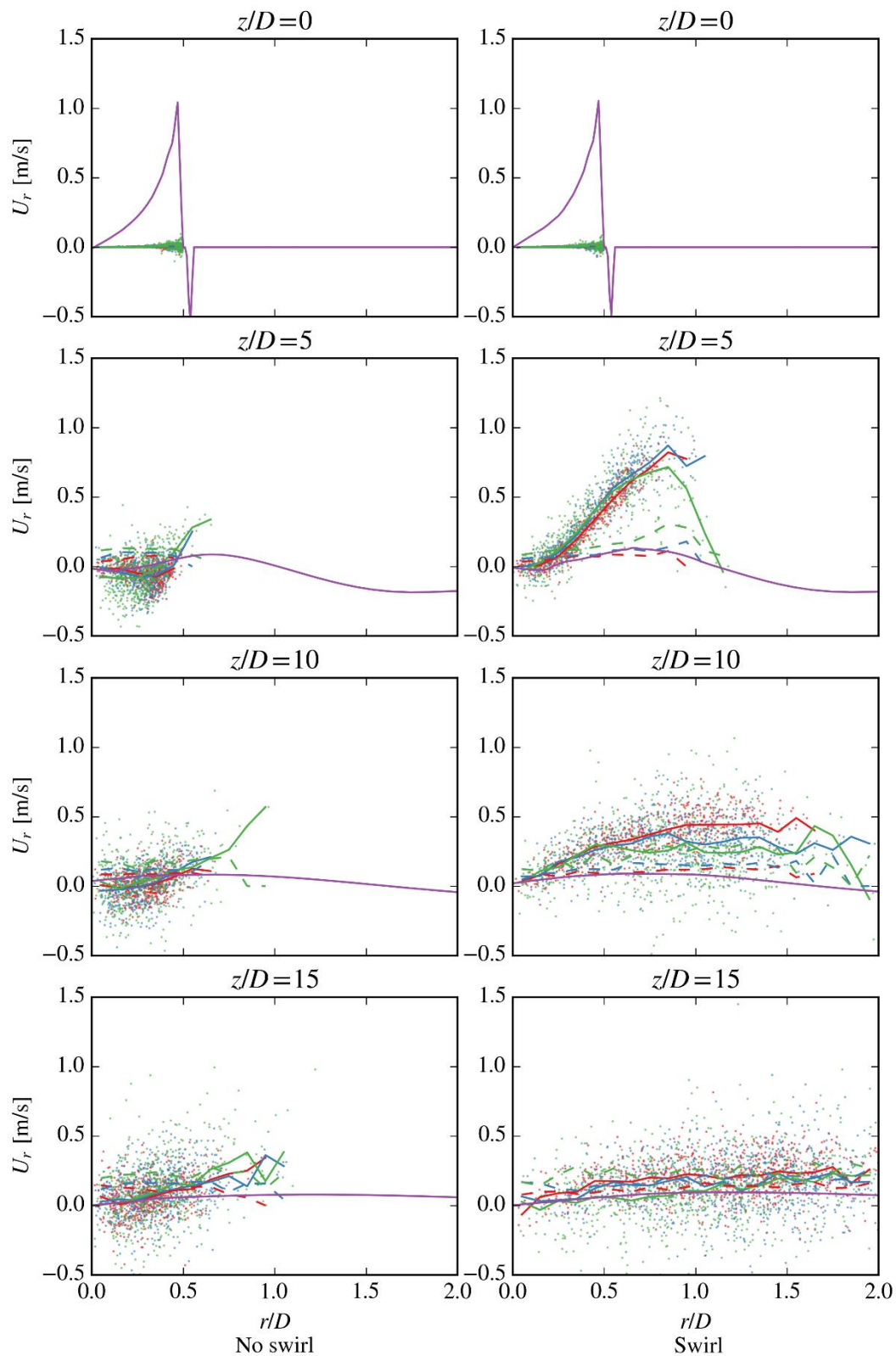
Fig. 10 Particle axial velocity distribution at $z/D = 15$ under non-swirl conditions. “Spheroid” means results are predicted by the spheroid model and “sphere” means results are predicted by the sphere model, the number indicates the initial orientations of spheroidal particles as stated in Fig. 2.



757

758 Fig. 11 Particle ages along reactor radius at different heights along the reactor (vertical) for non-
759 swirl and swirl conditions (horizontal). Solid line: averaged particle age; dash line: standard deviation
760 of particle age; scatter: particle age. Red: the sphere model; blue: the simplified non-sphere model;
761 green: the spheroid model.

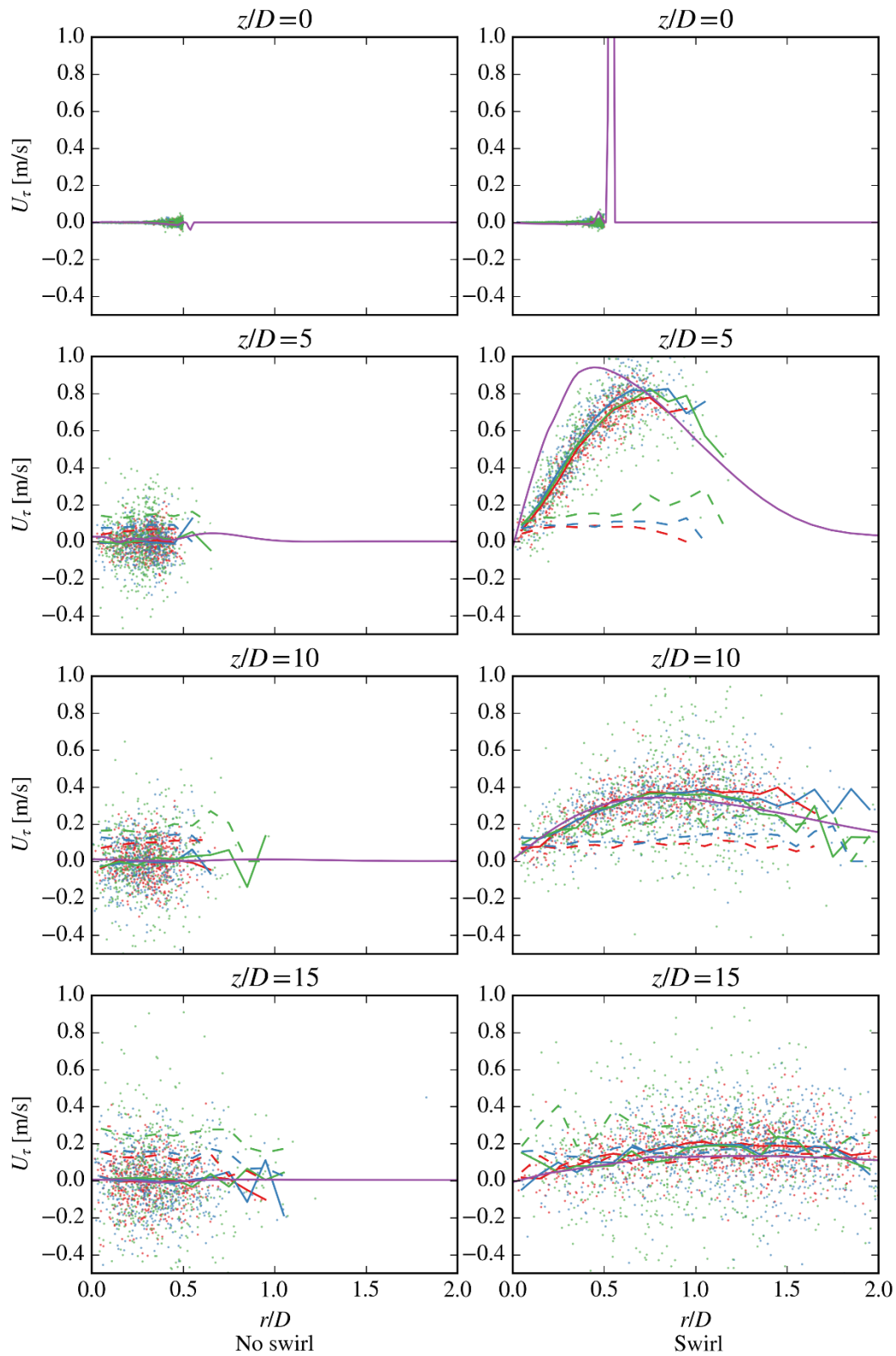
762



763

764 Fig. 12 Particle and fluid radial velocity distribution along reactor radius at different heights along
 765 the reactor (vertical) for non-swirl and swirl conditions (horizontal). Solid line: fluid or averaged
 766 particle velocity; dash line: standard deviation of particle velocity; scatter: particle velocity. Purple:
 767 fluid; red: the sphere model; blue: the simplified non-sphere model; green: the spheroid model.

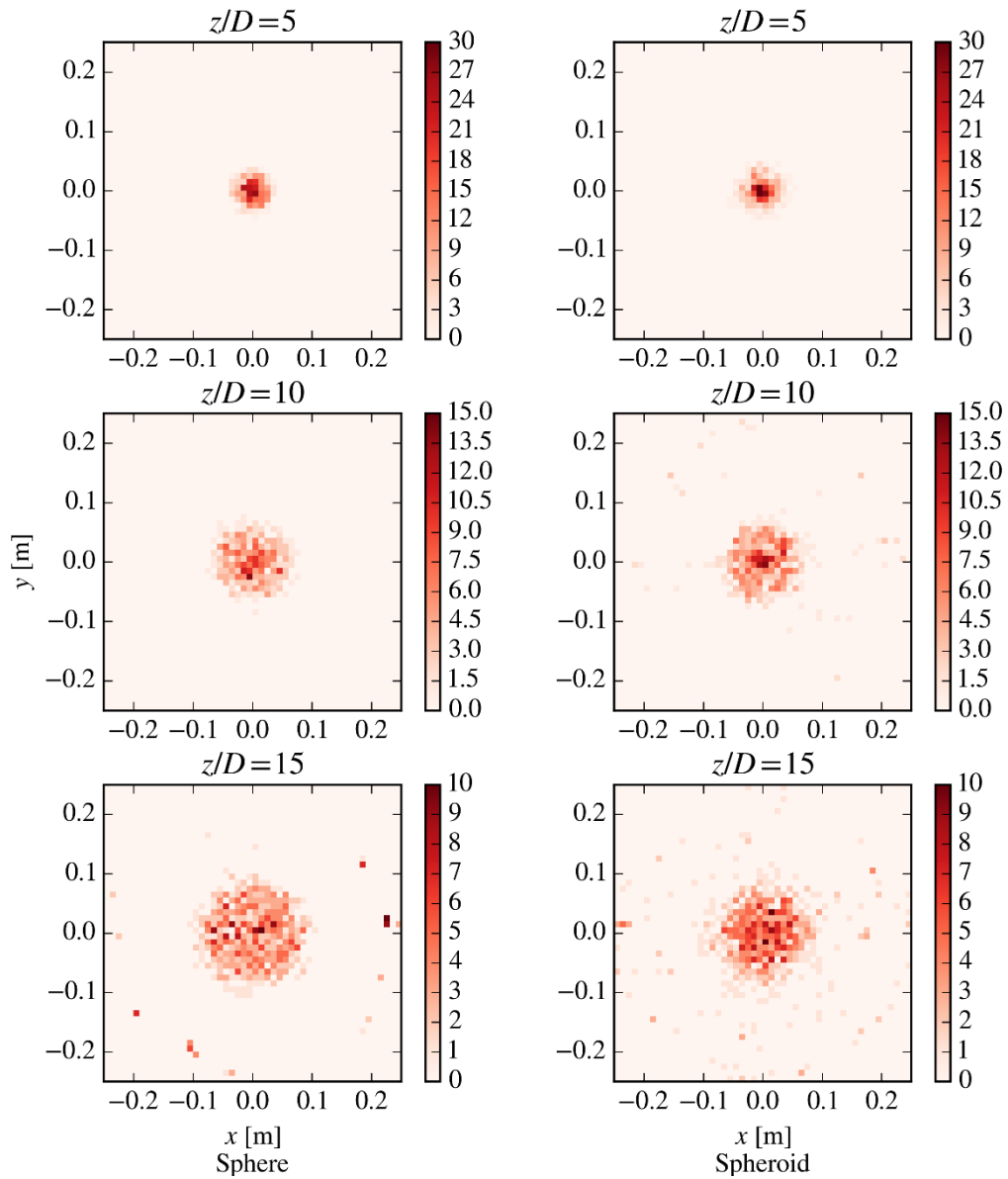
768



769

770 Fig. 13 Particle and fluid tangential velocity distribution along reactor radius at different heights
 771 along the reactor (vertical) for non-swirl and swirl conditions (horizontal). Solid line: fluid or averaged
 772 particle velocity; dash line: standard deviation of particle velocity; scatter: particle velocity. Purple:
 773 fluid; red: the sphere model; blue: the simplified non-sphere model; green: the spheroid model.

774



775

776 Fig. 14 Reactor cross-section indicating particle concentrations of swirl conditions at different
777 heights along the reactor (vertical) for the spherical and spheroidal particles (horizontal). The color bar
778 indicates the local concentration of particle i.e. number of particles per unit space, "sphere" and
779 "spheroid" means they are predicted by the sphere model and the spheroid model, respectively.

780

781

Table 1 Particle and fluid properties for model verification of torque

	Unit	Value
Particle aspect ratio	-	10
Particle radius of minor axis	m	0.001
Particle Stokes number (defined in [42])	-	10
Density ratio of particle to fluid	-	1000
Kinematic viscosity of fluid	m ² /s	0.1

782

783

784

Table 2 Particle and fluid properties for model verification of drag

	Unit	Experiments by Lau et al. [36]	Simulation
Particle diameter	μm	20 (with standard deviation less than 5%)	$a=20,$ $c=1.001a$
Particle mass loading factor	-	0.4	0.4
Jet exit diameter, D_{jet}	mm	12.7	12.7
Jet bulk velocity	m/s	12	12
Jet-to-co-flow velocity ratio	-	12	12
Stokes number (defined in [43])	-	1.4	1.4

785

786

787

Table 3 Simulation configurations for the simplified entrained flow reactor

	Unit	No swirl	Swirl
Air density	kg/m ³	1.205	1.205
Primary air volume flow rate	L/min	535	535
Secondary air volume flow rate	L/min	410	410
Secondary air rotation speed	RPM	0	3172
Particle density	kg/m ³	650	650
Particle equivalent diameter	μm	250	250
Particle mass flow rate	kg/h	20.2	20.2

788